# Interplay between crystal field and magnetic anisotropy in the triangular-lattice antiferromagnet $NaTmTe_2$

Shiyi Zheng,[1,*] Yiqing Gu,[1,*] Yimeng Gu,[1,*] Zeyu Kao,[1] Qisi Wang,[2] Hongliang Wo,[1] Yinghao Zhu,[1] Feiyang Liu,[1] Liusuo Wu,[3] Jieming Sheng,[3] Johan Chang,[4] Seiko Ohira-Kawamura,[5] Naoki Murai,[5] Christof Niedermayer,[6] Daniel Gabriel Mazzone,[6] Gang Chen,[7,8] and Jun Zhao[1,9,10,†]

[1]*State Key Laboratory of Surface Physics and Department of Physics, Fudan University, Shanghai 200433, China*
[2]*Department of Physics, The Chinese University of Hong Kong, Shatin, Hong Kong, China*
[3]*Department of Physics, Southern University of Science and Technology, Shenzhen 518055, China*
[4]*Physik-Institut, Universität Zürich, Winterthurerstrasse 190, CH-8057 Zürich, Switzerland*
[5]*Materials and Life Science Division, J-PARC Center, Tokai, Ibaraki 319-1195, Japan*
[6]*Laboratory for Neutron Scattering, Paul Scherrer Institut, CH-5232 Villigen, Switzerland*
[7]*International Center for Quantum Materials, School of Physics, Peking University, Beijing 100871, China*
[8]*Department of Physics and HKU-UCAS Joint Institute for Theoretical and Computational Physics at Hong Kong, The University of Hong Kong, Hong Kong, China*
[9]*Institute of Nanoelectronics and Quantum Computing, Fudan University, Shanghai 200433, China*
[10]*Shanghai Research Center for Quantum Sciences, Shanghai 201315, China*

(Received 20 November 2023; revised 31 January 2024; accepted 2 February 2024; published 26 February 2024)

We have successfully synthesized a triangular lattice magnet, $NaTmTe_2$, and conducted thermodynamic and inelastic neutron scattering (INS) investigations using single-crystal samples. Our magnetic susceptibility $\chi(T)$ measurements indicate antiferromagnetic interactions between $Tm^{3+}$ moments. In our INS experiments, we observe a series of dispersive crystal electric field (CEF) excitations. These dispersions could be attributed to quantum tunneling effects arising from anisotropic spin exchange interactions, spontaneously establishing connections between distinct CEF states. Additionally, the field-dependent behavior of the CEF states exhibits pronounced nonlinear characteristics, suggestive of quantum fluctuations within the rare-earth moments. Utilizing the mean field technology of the random phase approximation, we compute the magnetic excitation spectra and thermodynamic properties, unveiling the emergence of a unique ground state primarily driven by quantum effects.

DOI: 10.1103/PhysRevB.109.075159

## I. INTRODUCTION

Rare-earth compounds have served as fertile ground for the discovery of new phenomena, consistently attracting intense research interest over the years. In crystalline solids featuring $4f$ atomic orbitals, the spin-orbit coupling effect gives rise to an electronic multiplet that is described by a total angular momentum number $J$. The crystal electric field, influenced by surrounding ligands, further splits the originally degenerate spherical harmonic basis states. At low temperatures, the single-ion ground state of rare-earth moments can be occupied by low-lying degenerate or nearly degenerate crystal electric field (CEF) manifolds, leading to the emergence of collective quantum fluctuations and pronounced magnetic anisotropy. These conditions allow for the realization of various novel electronic states, such as the quantum spin liquid states [1–5], spin ice states [6–9], nematicity [10,11], and intertwined multipolar orders [12–16]. Consequently, there has been considerable interest in exploring exotic quantum phenomena in new rare-earth materials experimentally and theoretically.

Recently, studies of thulium-based antiferromagnets $TmMgGaO_4$ [15] and $KTmSe_2$ [17] have shown a unique ground state of local $Tm^{3+}$ moments, with unconventional magnetic excitations observed in neutron scattering measurements. In both compounds, the quantum tunneling effect induced by Ising interactions combines the two lowest CEF singlets into a ground state "quasidoublet," and the intertwined multipolar behaviors can be described with the transverse field Ising model (TFIM) [13]. In the language of TFIM, a long-range three-sublattice magnetic order coexists with the in-plane ferroquadrupole order in $TmMgGaO_4$ [15], while all the effective spins in $KTmSe_2$ are fully polarized by the intrinsic transverse field [17]. From another perspective, the two materials are located in the "order-by-disorder" state and "quantum disordered" state in the phase diagram of TFIM, respectively [14].

The successful applications of TFIM provide an ideal platform for realizing quantum states in non-Kramers compounds, where the low-temperature magnetism is completely different from the Kramers systems [2–4,18–23]. Importantly, simulations based on quantum Monte Carlo methods have predicted

*These authors contributed equally to this work.
†zhaoj@fudan.edu.cn

 

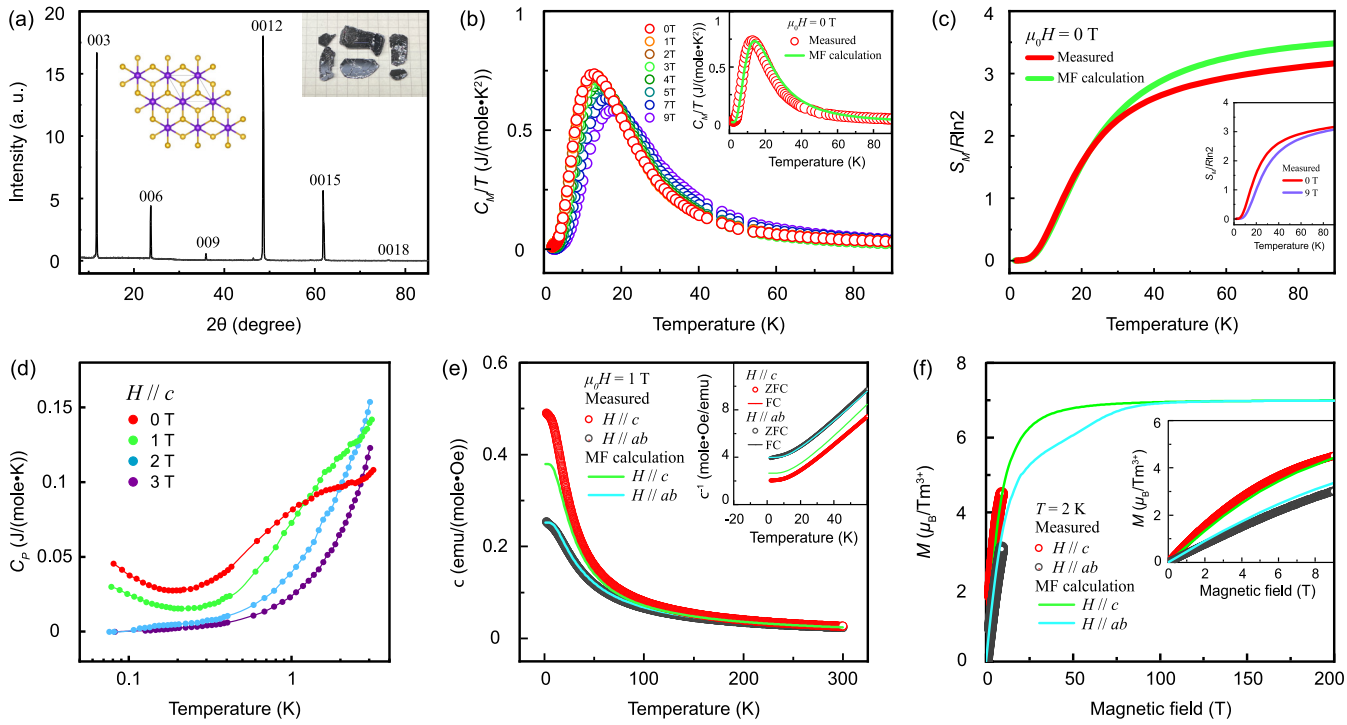


FIG. 1. (a) XRD pattern of a $NaTmTe_2$ single crystal on the $(0, 0, L)$ plane. The inset is an image of typical samples and schematic of the triangular lattice; purple: $Tm^{3+}$, brown: $Te^{2-}$. The nearest Tm-Tm and Tm-Te distances are 4.348 Å and 3.046 Å, respectively. (b) Corrected heat capacity after subtracting the heat capacity of $NaLuTe_2$ as phonon background, magnetic fields are applied along the $c$ axis. The inset shows simulated data under zero field. (c) Measured and simulated magnetic entropy release. (d) Heat capacity at extremely low temperatures. (e) Magnetic susceptibility from 1.8 K to 300 K in two directions under 1 T; no splitting is found between FC and ZFC data. The negative Curie-Weiss temperatures suggest predominately antiferromagnetic interactions. (f) Field dependence of magnetization at 2 K. In our measurements up to 9 T no saturation of $Tm^{3+}$ moment was observed. From mean field calculation, the out-of-plane component $M_c$ saturates upon 60 T, while the in-plane component $M_{ab}$ first increases linearly with fields between 30 T to 70 T, then saturates above 100 T.

a quantum critical point (QCP) in TFIM, at which the quantum tunneling lifts the macroscopic degeneracies and therefore stabilizes a long-range ordered state [14]. However, the exact position of the QCP in the phase diagram still awaits experimental verification. Furthermore, given the strong correlation between the effective transverse field and the magnitude of spin exchange interactions with lattice parameters [13,14], it becomes intriguing to expand this research to include a broader range of isostructural compounds through ligand substitution.

In this paper, we have successfully synthesized a delafossite compound, $NaTmTe_2$, and conducted a comprehensive investigation using single-crystal samples. In Sec. II, we introduce the experimental details, including sample synthesis, x-ray diffraction, and thermodynamic measurements. In Sec. III, we illustrate the inelastic neutron scattering data on single-crystalline $NaTmTe_2$ samples. In Sec. IV, we provide simulated results based on the random phase approximation (RPA) method. In Sec. V, we conclude with a discussion.

## II. SAMPLE PREPARATION AND THERMODYNAMIC PROPERTIES

The synthesis of polycrystalline $NaTmTe_2$ samples was carried out through a solid-state reacting method. High-quality starting elements, with a molar ratio of Na : Tm : Te = 1 : 1 : 2, were sealed within evacuated quartz tubes and heated to 1050 °C for 3 days. Single-crystalline $NaTmTe_2$ samples were grown using $Na_2Te_3$ as a fluxing agent. A powder mixture of $NaTmTe_2$ and $Na_2Te_3$ in a ratio of 1:10 was placed in alumina crucibles and heated to 1050 °C for 5 hours. The temperature was then gradually reduced to 650 °C at a rate of 0.8 °C/h, at which temperature the extra flux was removed via centrifuge. The resulting single-crystalline $NaTmTe_2$ exhibits a hexagonal form with well-defined edges [Fig. 1(a) inset]. The XRD measurements were conducted using a Bruker D8 Discover diffractometer with Cu $K_\alpha$ radiation. The collected XRD powder diffraction data were refined using the FULLPROF SUITE software [24], based on which we extract detailed information about crystal parameters and structure [Fig. 1(a)]. A summary of the pertinent crystallographic parameters for the $NaTmTe_2$ compound is provided in Table I. With the space group $R$-3$m$, the magnetic $Tm^{3+}$ moments in $NaTmTe_2$ form quasi-two-dimensional triangular-lattice layers, characterized by strong geometrical frustration [25].

The thermodynamic properties and magnetic features were obtained using a PPMS DynaCool instrument with a 9 T magnet (Quantum Design). The corrected magnetic heat capacity $C_M$ and magnetic entropy release $S_M$ are depicted in Fig. 1(b) and Fig. 1(c), respectively, after subtracting the phonon background estimated from measurements on $NaLuTe_2$, with the external fields applied along the crystalline $c$ axis. Below 0.3 K, we can observe a Schottky-like increase [Fig. 1(d)].

TABLE I. Refined crystallographic parameters from room-temperature x-ray powder diffraction.

| $NaTmTe_2$ polycrystalline sample (Trigonal, space group $R$-3$m$, $Z = 3$) | |
|---|---|
| Lattice parameters | |
| $a$ (Å) | 4.34833(1) |
| $b$ (Å) | 4.34833(1) |
| $c$ (Å) | 22.4293(5) |
| $V$ (Å$^3$) | 367.274(9) |
| $\alpha$ (deg) | 90 |
| $\beta$ (deg) | 90 |
| $\gamma$ (deg) | 120 |

Therefore, no discernible phase transition can be observed in heat capacity measurements, indicating the absence of long-range magnetic order in $NaTmTe_2$ under zero or external fields.

A comprehensive overview of the DC susceptibility $\chi$ under 1 T is presented in Fig. 1(e). There is no splitting between zero-field-cooled (ZFC) and field-cooled (FC) data at low temperatures, precluding the possibility of a magnetic order. The in-plane magnetic response of $Tm^{3+}$ ions is slightly weaker than the out-of-plane response, suggesting a moderate anisotropy. The inverse susceptibility exhibits Curie-Weiss (CW) behavior, following the formula $\chi = C/(T - \theta)$ above 20 K. The extracted Curie-Weiss temperatures ($\theta_c = -3.414$ K and $\theta_{ab} = -17.303$ K) observed in the temperature range of 30 K to 60 K strongly suggest the antiferromagnetic (AFM) spin interactions [Fig. 1(e) inset]. The corresponding effective magnetic moments ($\mu^c_{\text{eff}} = 8.25\ \mu_B$ and $\mu^{ab}_{\text{eff}} = 7.96\ \mu_B$), fitted as $\sqrt{8C}$, are slightly larger than the ideal value for a free $Tm^{3+}$ moment ($\mu_{\text{free}} = g_J\sqrt{J(J+1)}\ \mu_B = 7.57\ \mu_B$) [26]. No saturation phenomenon of $Tm^{3+}$ moments was observed up to 9 T in our magnetization measurements [Fig. 1(f)]; further theoretical simulations on the Van Vleck paramagnetic contribution $\chi_0$ will be introduced in Sec. IV.

## III. INELASTIC NEUTRON SCATTERING MEASUREMENTS

Unlike $TmMgGaO_4$ [15,16] and $KTmSe_2$ [17], the magnetic anisotropy observed in $NaTmTe_2$ notably deviates from Ising behavior, suggesting the presence of a distinct CEF ground state in $NaTmTe_2$ [27,28]. To gain insights into the CEF structure and spin exchange parameters, we conducted neutron scattering measurements to unveil the magnetic excitation spectra.

Inelastic neutron scattering measurements under zero field were carried out on the AMATERAS cold neutron disk chopper spectrometer at the Japan Proton Accelerator Research Complex [29]. Utilizing 2.5 grams of single-crystalline samples co-aligned in the $(H, K, 0)$ scattering plane, the collected data were analyzed with the HORACE program [30]. To safeguard the single-crystalline $NaTmTe_2$ samples from the detrimental effects of air and moisture, we applied CYTOP glue as a protective coating.

At a base temperature of 80 mK, the neutron diffraction data do not reveal any magnetic Bragg peak, providing clear evidence of the absence of long-range magnetic order in $NaTmTe_2$, consistent with the findings in the heat capacity measurements. In the inelastic channel with incident energy of $E_i = 7.7$ meV, two branches of magnetic excitations are identified. The excitation from CEF ground state to the first excited state at ∼3 meV is highly dispersive in the reciprocal space, suggesting that the local environment of $Tm^{3+}$ moments extends beyond single-ion level and is coupled with spin exchange interactions [Fig. 2(a)]. The momentum-dependent spectral intensity clearly illustrates dispersion of the first branch of excitation in Fig. 2(a): the excitation initially emerges at 2.7 meV and disperses outward from the $K$ points, then forms hexagonal patterns around the Γ points before disappearing above 3.2 meV [Figs. 3(a)–3(f)]. With an increase in temperature (40 K), the excitations become weaker and flatter due to the thermal effect [Fig. 2(b)]. The second branch (excitation from ground state to the 2nd state) at ∼4.3 meV is less dispersive, possibly due to weaker exchange-CEF interplay. With $E_i = 15$ meV, three additional excited states are observed at 80 mK [Fig. 2(c)], with an intensity approximately two orders of magnitude weaker than the two other states [Fig. 2(g)].

The magnetic field effect on CEF states was investigated on the CAMEA multiplexing neutron spectrometer at the Swiss spallation neutron source of the Paul Scherrer Institute [31]; the obtained data were analyzed with the MJOLNIR program [32]. The $NaTmTe_2$ samples were co-aligned in the same scattering plane, while the external fields were applied along the $c$ direction. The CEF states exhibit slight alterations under 2 T [Fig. 4(b)], while the spectral weight shifts to higher energies under 6 T [Fig. 4(c)]. Importantly, the nonlinear field dependence of CEF states is inconsistent with the conventional Zeeman effect, evidenced by a group of constant-$Q$ cuts [Fig. 4(d)].

## IV. SIMULATIONS AND DISCUSSION

In $NaTmTe_2$, the $D_{3d}$ local point symmetry lifts the $(2J+1)$-fold degenerate $^3H_6$ multiplet states of $Tm^{3+}$ moments into several nondegenerate states due to the strong spin-orbit coupling. To initiate our analysis, the first essential step is to fit the CEF states as observed in INS measurements. Since the CEF excitations are dispersive in reciprocal space, we selected a relatively wide integral range to obtain the energy levels: $0 < q_x < 1.5$, $-1 < q_y < 1$, $-1 < q_z < 1$; here $x, y, z$ represent the $[H, 0, 0]$, $[-K, 2K, 0]$, and $[0, 0, L]$ directions, respectively, as shown in Fig. 2(g). The CEF parameters of $NaTmTe_2$ were determined using the CEF Hamiltonian given by

$$\hat{\mathcal{H}}_{\text{CEF}} = \sum_{n,m} B^m_n \hat{O}^m_n, \tag{1}$$

where $\hat{O}^m_n$ are the Stevens operators and $B^m_n$ are multiplicative factors called the CEF parameters [33]. Under the $D_{3d}$ point symmetry, only six CEF parameters are allowed to be nonzero in [Eq. (1)]: $B^0_2$, $B^0_4$, $B^3_4$, $B^0_6$, $B^3_6$, and $B^6_6$. An initial estimate of $B^0_{2,\text{est}} = -0.004$ meV is obtained from high-temperature

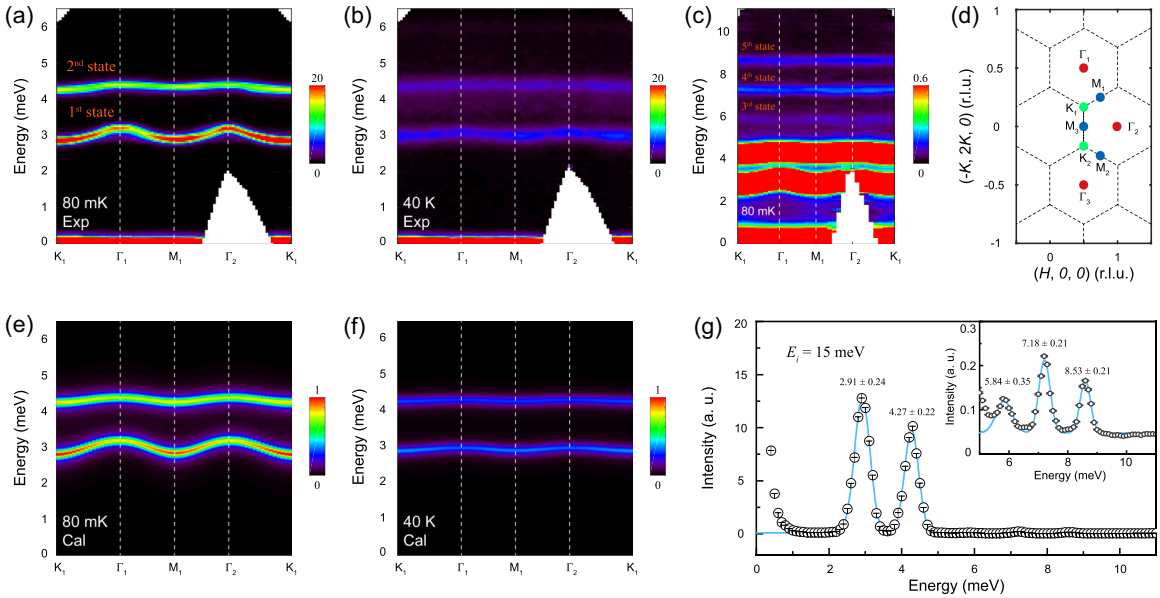


FIG. 2. Measured magnetic excitation spectra along a high-symmetry path at 80 mK (a) and 40 K (b); the incident energy is $E_i = 7.7$ meV. At low temperature, the CEF states are dispersive, suggesting strong coupling between CEF and spin exchange interactions. With increasing temperature, the excitations become weaker and less dispersive. (c) Magnetic excitation spectrum at 80 mK with $E_i = 15$ meV; three more CEF states are observed by reducing intensity scale. (d) Sketch of the reciprocal space; dashed lines indicate the Brillouin zone boundaries. (e), (f) Simulated spectra through the RPA method as described in text. (g) Energy dependence of the magnetic excitation spectrum at 80 mK; solid lines denote Gaussian fit of the peaks, energy width of the fitted peaks is close to the experimental energy resolution, and the error bars denote the standard deviation. INS experiments under zero field were performed on 2.5 g single-crystalline $NaTmTe_2$ samples on the time-of-flight spectrometer AMATERAS; color bars denote scattering intensity in arbitrary units in linear scale.

susceptibility [34],

$$\theta_{ab} - \theta_c = \left(\frac{6B_2^0}{5k_B}\right)\left(J - \frac{1}{2}\right)\left(J + \frac{3}{2}\right). \tag{2}$$

Here the CW temperatures $\theta_{ab}$ and $\theta_c$ are fitted in a high-$T$ range (200 K to 300 K); $J = 6$ denotes the total angular momentum of $Tm^{3+}$.

We used the McPhase software package to fit the integrated peaks [35]. The calculated eigenvectors of Eq. (1) are shown in Table II, and the optimized CEF parameters and eigenvalues

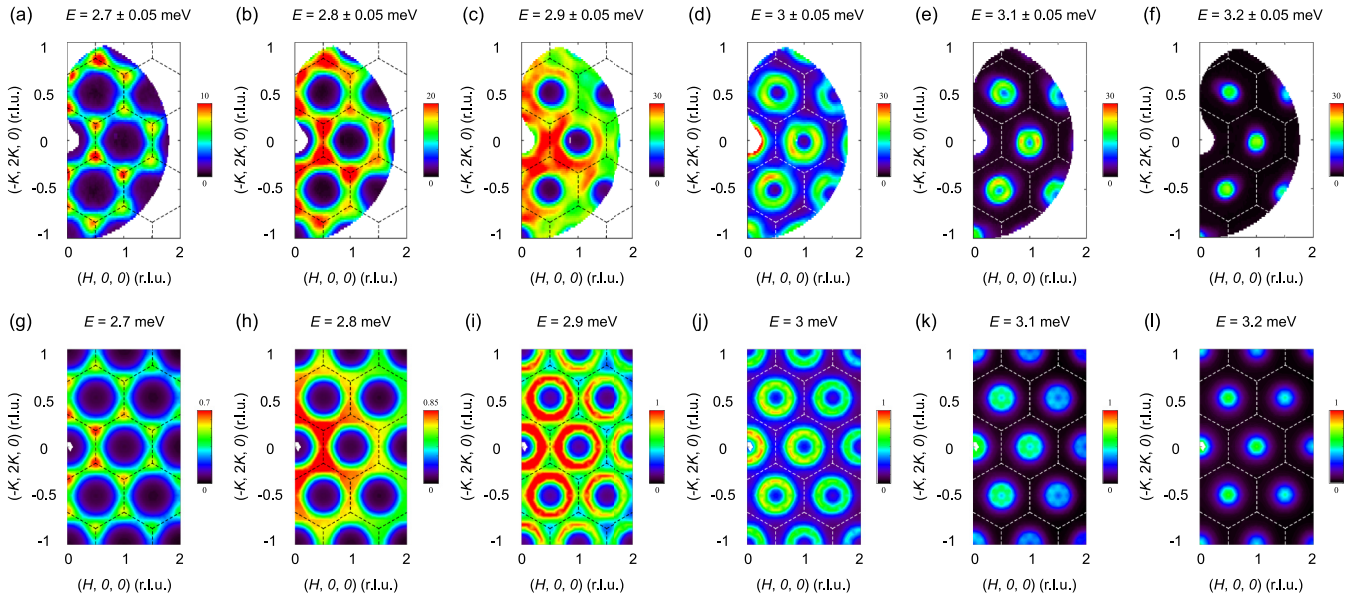


FIG. 3. (a)–(f) Measured momentum dependence of the dispersive CEF excitation at the indicated energies with $E_i = 7.7$ meV and $T = 80$ mK. (g)–(l) Simulated results through the RPA method. The dashed lines indicate the zone boundaries and the color bars denote scattering intensity in arbitrary units in linear scale.

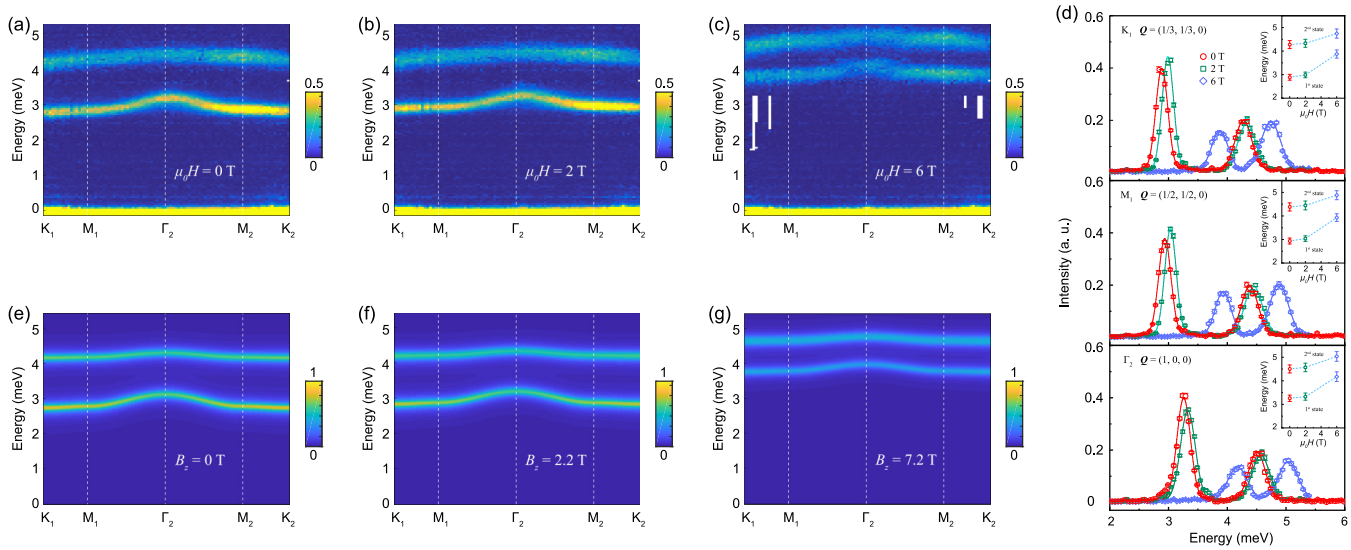


FIG. 4. (a)–(c) CEF excitations measured under 0 T, 2 T, 6 T, respectively; $T = 36$ mK. The field dependence of CEF states was performed on the multiplexing triple-axis spectrometer CAMEA with $E_i = 5$, 6.8, 8.6 meV. (d) Constant-momentum cuts at high-symmetry points in the reciprocal space; solid lines denote Gaussian fit of the peaks, a.u. denotes arbitrary units, and error bars denote the standard deviation. (e)–(g) Simulated results through the RPA method by adding a Zeeman term into the effective magnetic Hamiltonian. Notice that the fitted fields are a bit larger than the applied fields in measurements, suggesting collective quantum effects.

are listed in Table III, which are consistent with INS results. The absence of an excited state at ∼10.7 meV in INS could be due to the weak scattering intensity. Previous theoretical analysis has predicted that the 13-fold ($J = 6$, $L = 5$, $S = 1$) degenerate ground state of the free $Tm^{3+}$ moment ($4f^{12}$ configuration) would split into five singlets and four doublets under the $D_{3d}$ CEF environment, which agrees with our results [16].

In our INS measurements, the dispersion in magnetic excitation spectra indicates strong interplay between CEF and spin exchange interactions, extending beyond the scope of single-ion considerations [Fig. 2(a)]. To describe the dispersive modes, we expanded the CEF Hamiltonian into an effective magnetic Hamiltonian, accounting for the effective moments and anisotropic exchange interactions simultaneously. When establishing the Hamiltonian, an XXZ model is adopted due to the quasi-2D nature of $NaTmTe_2$ [1,2,21,22],

$$\begin{aligned}\hat{\mathcal{H}}_{\text{eff}} &= \hat{\mathcal{H}}_{\text{CEF}} + \hat{\mathcal{H}}_{\text{spin}} \\ &= \sum_{n,m} B_n^m \hat{O}_n^m + \sum_{\langle i,j \rangle} J_{xy}\left(\hat{J}_i^x \hat{J}_j^x + \hat{J}_i^y \hat{J}_j^y\right) + J_z \hat{J}_i^z \hat{J}_j^z, \quad (3)\end{aligned}$$

where $J_{xy}$ and $J_z$ represent the nearest in-plane and out-of-plane exchange parameters, respectively; $\hat{J}_i$ and $\hat{J}_j$ describe the original $J = 6$ operators of the $Tm^{3+}$ moment. Based on $\hat{\mathcal{H}}_{\text{eff}}$, McPhase uses the RPA method to simulate the dispersive CEF excitations by using a set of AFM exchange parameters: $J_{xy} = 0.0012$ meV and $J_z = 0.0031$ meV. Here we found that $J_z$ and $J_{xy}$ are coupled to the first and second branch of magnetic excitations, respectively, while the higher excited states are barely affected by exchange effect. In this picture, the anisotropic exchange interactions between $Tm^{3+}$ moments will induce strong quantum tunneling effect between distinct CEF states, resulting in the unique ground state associated with dispersive excitations. The simulated *E-k* and momentum dependence results at 80 mK are shown in Fig. 2(e) and Figs. 3(g)–3(l), in agreement with experimental data. We have further extended our analysis by simulating the excitation spectrum at 40 K, utilizing the same set of CEF and anisotropic exchange parameters. This simulation, as shown in Fig. 2(f), demonstrates consistency with the inelastic

TABLE II. Calculated eigenvectors of the CEF Hamiltonian in the $J^z$ basis [Eq. (1)]. Here $|\Psi_{n,\pm}\rangle$ represents a CEF excited state doublet consisting of $|\Psi_{n,+}\rangle$ and $|\Psi_{n,-}\rangle$.

| Eigenstate | Eigenvector |
|---|---|
| $\|\Psi_0\rangle$ | $-0.347(\|6\rangle + \|-6\rangle) - 0.612(\|3\rangle + \|-3\rangle) - 0.096\|0\rangle$ |
| $\|\Psi_1\rangle$ | $-0.592(\|6\rangle - \|-6\rangle) - 0.385(\|3\rangle - \|-3\rangle) - 0.020\|0\rangle$ |
| $\|\Psi_{2,\pm}\rangle$ | $\pm 0.067\|\pm 5\rangle \pm 0.11\|\pm 4\rangle \mp 0.82\|\pm 2\rangle - 0.022\|\pm 1\rangle \pm 0.103\|\mp 1\rangle \pm 0.174\|\mp 2\rangle + 0.518\|\mp 4\rangle - 0.014\|\mp 5\rangle$ |
| $\|\Psi_3\rangle$ | $0.615(\|6\rangle + \|-6\rangle) - 0.348(\|3\rangle + \|-3\rangle) - 0.004\|0\rangle$ |
| $\|\Psi_4\rangle$ | $0.348(\|6\rangle - \|-6\rangle) - 0.524(\|3\rangle - \|-3\rangle) - 0.454\|0\rangle$ |
| $\|\Psi_{5,\pm}\rangle$ | $\mp 0.128\|\pm 5\rangle \pm 0.336\|\pm 4\rangle \pm 0.31\|\pm 2\rangle + 0.438\|\pm 1\rangle + 0.569\|\mp 1\rangle \mp 0.238\|\mp 2\rangle - 0.436\|\mp 4\rangle \mp 0.098\|\mp 5\rangle$ |
| $\|\Psi_{6,\pm}\rangle$ | $0.272\|\pm 5\rangle \pm 0.368\|\pm 4\rangle - 0.293\|\pm 2\rangle - 0.343\|\pm 1\rangle \pm 0.484\|\mp 1\rangle \mp 0.207\|\mp 2\rangle + 0.519\|\mp 4\rangle - 0.193\|\mp 5\rangle$ |
| $\|\Psi_7\rangle$ | $-0.167(\|6\rangle - \|-6\rangle) - 0.283(\|3\rangle + \|-3\rangle) - 0.885\|0\rangle$ |
| $\|\Psi_{8,\pm}\rangle$ | $\mp 0.87\|\pm 5\rangle \mp 0.033\|\pm 4\rangle - 0.111\|\pm 2\rangle + 0.117\|\pm 1\rangle \pm 0.324\|\mp 1\rangle \pm 0.04\|\mp 2\rangle + 0.092\|\mp 4\rangle - 0.316\|\mp 5\rangle$ |

TABLE III. CEF parameters and eigenvalues simulated from CEF Hamiltonian of $NaTmTe_2$. Resolution of energy in inelastic neutron scattering with $E_i = 15$ meV is ~0.2 meV.

| CEF parameter $B_n^m$ | Simulation (meV) |
|---|---|
| $B_2^0$ | $-5.858(9) \times 10^{-3}$ |
| $B_4^0$ | $-1.613(7) \times 10^{-4}$ |
| $B_4^3$ | $-1.815(2) \times 10^{-5}$ |
| $B_6^0$ | $-1.435(5) \times 10^{-5}$ |
| $B_6^3$ | $-7.851(2) \times 10^{-5}$ |
| $B_6^6$ | $-6.212(1) \times 10^{-5}$ |
| Observed level (meV) | Eigenvalue (meV) |
| 0 | 0 ($\|\Psi_0\rangle$) |
| $2.91 \pm 0.24$ | 2.909(2) ($\|\Psi_1\rangle$) |
| $4.27 \pm 0.22$ | 4.298(1) ($\|\Psi_{2,\pm}\rangle$) |
| $5.84 \pm 0.35$ | 5.896(8) ($\|\Psi_3\rangle$) |
| $7.18 \pm 0.21$ | 7.104(8) ($\|\Psi_4\rangle$) |
| $8.53 \pm 0.21$ | 8.436(6) ($\|\Psi_{5,\pm}\rangle$) |
| Not observed | 10.708(4) ($\|\Psi_{6,\pm}\rangle$) |
| Not observed | 13.450(7) ($\|\Psi_7\rangle$) |
| Not observed | 15.406(1) ($\|\Psi_{8,\pm}\rangle$) |

neutron scattering data, reinforcing the validity of our chosen parameters.

Having determined the CEF splitting and anisotropic exchange parameters in $NaTmTe_2$, we can simulate the corresponding heat capacity, entropy release, susceptibility, and magnetization (Fig. 1). Our results corroborated the AFM spin relations between $Tm^{3+}$ local moments in both directions, consistent with the susceptibility measurements. The slight discrepancy in $\chi_c$ between experimental data and simulation may be attributed to a potential error in the sample weighing process [Fig. 1(e)]. In magnetization measurements, no saturation phenomena were observed due to the restriction of external fields. From MF simulations, we found that the out-of-plane component of the $Tm^{3+}$ moment $M_c$ becomes saturated at approximately 60 T, while the in-plane component $M_{ab}$ increases linearly between 30 T and 70 T before fully saturating upon 100 T. Therefore, we can deduce the Van Vleck parameters $\chi_0^{ab} = 0.0299\ \mu_B/T$ and $\chi_0^c = 0.0005\ \mu_B/T$ [Fig. 1(f)]. Subsequently, we corrected the CW temperatures using the refined CW law $\chi - \chi_0 = C/(T - \theta)$, accounting for paramagnetic effects. The adjusted values are $\theta_{ab} = -10.575$ K, $\theta_c = -4.801$ K, while the simulated effective moments $\mu_{\text{eff}}^{ab} = 7.04\ \mu_B$ and $\mu_{\text{eff}}^{c} = 7.84\ \mu_B$ are more reasonable and much closer to the free moment $\mu_{\text{free}} = 7.57\ \mu_B$ comparing to experimental results.

It is interesting to draw a comparison between $NaTmTe_2$ and two other triangular-lattice thulium-based compounds, $TmMgGaO_4$ and $KTmSe_2$. In $TmMgGaO_4$, the two lowest CEF singlets are combined to a ground state quasidoublet with a gap of $\Delta E_{\text{TMGO}} = 0.62$ meV [15]. Such an exotic ground state originates from quantum tunneling induced by Ising interactions, giving rise to an effective spin-$\frac{1}{2}$ [16]. In another compound, $KTmSe_2$, the Ising anisotropy and ground state quasidoublet are well preserved. The intrinsic quantum fluctuation, however, is weaker than in $TmMgGaO_4$ due to a larger gap $\Delta E_{\text{KTS}} = 1.17$ meV, failing to stabilize a long-range magnetic order even at 60 mK [17]. Similarly to the previous two materials, eigenvectors of the two lowest CEF states in $NaTmTe_2$ are both singlets dominated by $|J^z = \pm 6\rangle$ and $|J^z = \pm 3\rangle$,

$$|\Psi_0\rangle = -0.347(2)(|6\rangle + |-6\rangle) - 0.612(2)(|3\rangle + |-3\rangle) - 0.096(3)|0\rangle, \quad (4)$$

$$|\Psi_1\rangle = -0.592(6)(|6\rangle - |-6\rangle) - 0.385(3)(|3\rangle - |-3\rangle) - 0.020(7)|0\rangle. \quad (5)$$

Here, the CEF ground state $|\Psi_0\rangle$ and the 1st excited state $|\Psi_1\rangle$ are connected through the out-of-plane exchange interaction via $\langle\Psi_0|\hat{J}_z|\Psi_1\rangle \neq 0$, generating the dispersion in the exciton-like excitation between these two CEF singlets. This explains why the momentum-dependent spectral intensity shown in Fig. 3 is so similar to the case of $TmMgGaO_4$ [15] and $KTmSe_2$ [17].

The magnitude of transverse field in TFIM is directly determined by CEF splitting, and can be mapped to the energy gap between $|\Psi_0\rangle$ and $|\Psi_1\rangle$. Therefore, the in-plane polarization effect in $NaTmTe_2$ is supposed to be stronger than in $TmMgGaO_4$ and $KTmSe_2$, suppressing the existence of long-ranged magnetic order [13,14]. However, the in-plane exchange component $\hat{J}_{xy}$ in $NaTmTe_2$ will further connect $|\Psi_0\rangle$ to $|\Psi_{2,\pm}\rangle$ ($\langle\Psi_0|\hat{J}_{xy}|\Psi_{2,\pm}\rangle \neq 0$), driving the system partially deviated from an ideal transverse field Ising model. Such type of connection hardly exists in $TmMgGaO_4$ and $KTmSe_2$ due to the difference in magnetic anisotropy. As a matter of fact, $NaTmTe_2$ demonstrates a unique ground state consisting of two singlets and one doublet, instead of a quasidoublet.

Finally, we explain the magnetic field dependence effect on CEF states (Fig. 4). Conventionally, we need to add a Zeeman term $\hat{\mathcal{H}}_{\text{Zeeman}}$ into the effective Hamiltonian,

$$\hat{\mathcal{H}}_{\text{eff}} = \hat{\mathcal{H}}_{\text{CEF}} + \hat{\mathcal{H}}_{\text{spin}} - \mu_B \sum_{\langle i \rangle} g_{\parallel} \hat{B}_z \hat{J}_i^z. \quad (6)$$

Here $\hat{B}_z$ is the effective field along the $c$ direction. We found the Zeeman splitting of the 2nd CEF state under 6 T is smaller than 0.1 meV which cannot be distinguished in the current INS data. Additionally, the simulated fields are a bit larger than the applied ones in experiments [Figs. 4(e)–4(g)], consistent with the nonlinear response of the $Tm^{3+}$ moment to external fields [Fig. 4(d)]. Such anomaly is commonly found in rare-earth systems [36] and originates from connections between CEF states in our case. In $NaTmTe_2$, the CEF ground state and excited states are connected through the quantum tunneling effect induced by anisotropic exchange interactions. Despite the absence of long-range magnetic order, the highly entangled ground state of the $Tm^{3+}$ moment will still give rise to non-ignorable quantum fluctuation [37], resulting in the experimental results and deviation from mean field calculations. Generally, such quantum fluctuations could be suppressed when the external fields are large enough.

## V. CONCLUSION

In summary, we have successfully synthesized a triangular-lattice rare-earth compound, $NaTmTe_2$, and conducted a comprehensive study of its low-temperature magnetism through a

combination of thermodynamic and neutron scattering measurements on high-quality single-crystalline samples.

In our INS experiments, we have observed the presence of five CEF excitations under zero field. The dispersion of these excitations suggests a strong interplay between the CEF and spin exchange interactions. Through the RPA simulations, we have identified a set of best-fitted parameters in the effective spin Hamiltonian that aligns well with our experimental findings. Unlike two other similar compounds, $TmMgGaO_4$ and $KTmSe_2$, where the ground state of the $Tm^{3+}$ moments is dominated by Ising interactions, the presence of quantum tunneling effects associated with anisotropic spin exchange interactions in $NaTmTe_2$ leads to the emergence of a distinct ground state.

Furthermore, the nonlinear field dependence of CEF excitations in our observations suggests the existence of quantum fluctuations, originating from connections between nondegenerate CEF states. These findings emphasize the pivotal role of quantum tunneling effects in shaping the ground state of non-Kramers moments, resulting in the manifestation of exotic low-temperature quantum phenomena.

## ACKNOWLEDGMENTS

We thank Dr. Devashibhai T. Adroja for providing valuable suggestions on the CEF fitting progress. This work is supported by the Key Program of the National Natural Science Foundation of China (Grant No. 12234006), National Key R&D Program of China (Grant No. 2022YFA1403202), and the Shanghai Municipal Science and Technology Major Project (Grant No. 2019SHZDZX01). Q.W. is supported by the Research Grants Council of Hong Kong (ECS No. 24306223). H.W. is supported by the Youth Foundation of the National Natural Science Foundation of China (Grant No. 12204108). Y.Z. is supported by the Youth Foundation of the National Natural Science Foundation of China (Grant No. 12304173). G.C. is supported by the Ministry of Science and Technology of China (Grant No. 2021YFA1400300), the National Science Foundation of China (Grant No. 92065203), and the Research Grants Council of Hong Kong (Grant No. C7012-21GF). The experiment at AMATERAS was carried out under approval of J-PARC Center (Proposal No. 2022B0129).

[1] Y. Li, G. Chen, W. Tong, L. Pi, J. Liu, Z. Yang, X. Wang, and Q. Zhang, Rare-earth triangular lattice spin liquid: A single-crystal study of $YbMgGaO_4$, Phys. Rev. Lett. **115**, 167203 (2015).

[2] Y. Shen, Y.-D. Li, H. Wo, Y. Li, S. Shen, B. Pan, Q. Wang, H. C. Walker, P. Steffens, M. Boehm, Y. Hao, D. L. Quintero-Castro, L. W. Harriger, M. D. Frontzek, L. Hao, S. Meng, Q. Zhang, G. Chen, and J. Zhao, Evidence for a spinon Fermi surface in a triangular-lattice quantum-spin-liquid candidate, Nature (London) **540**, 559 (2016).

[3] Y. Li, D. Adroja, P. K. Biswas, P. J. Baker, Q. Zhang, J. Liu, A. A. Tsirlin, P. Gegenwart, and Q. Zhang, Muon spin relaxation evidence for the U(1) quantum spin-liquid ground state in the triangular antiferromagnet $YbMgGaO_4$, Phys. Rev. Lett. **117**, 097201 (2016).

[4] J. A. M. Paddison, M. Daum, Z. Dun, G. Ehlers, Y. Liu, M. B. Stone, H. Zhou, and M. Mourigal, Continuous excitations of the triangular-lattice quantum spin liquid $YbMgGaO_4$, Nat. Phys. **13**, 117 (2017).

[5] Y. Shen, Y.-D. Li, H. C. Walker, P. Steffens, M. Boehm, X. Zhang, S. Shen, H. Wo, G. Chen, and J. Zhao, Fractionalized excitations in the partially magnetized spin liquid candidate $YbMgGaO_4$, Nat. Commun. **9**, 4138 (2018).

[6] B. C. den Hertog and M. J. P. Gingras, Dipolar interactions and origin of spin ice in Ising pyrochlore magnets, Phys. Rev. Lett. **84**, 3430 (2000).

[7] S. T. Bramwell and M. J. P. Gingras, Spin ice state in frustrated magnetic pyrochlore materials, Science **294**, 1495 (2001).

[8] J. E. Greedan, Frustrated rare earth magnetism: Spin glasses, spin liquids and spin ices in pyrochlore oxides, J. Alloys Compd. **408-412**, 444 (2006).

[9] M. J. P. Gingras and P. A. McClarty, Quantum spin ice: A search for gapless quantum spin liquids in pyrochlore magnets, Rep. Prog. Phys. **77**, 056501 (2014).

[10] H. S. Jeevan, C. Geibel, and Z. Hossain, Quasiquartet crystal-electric-field ground state with possible quadrupolar ordering in the tetragonal compound $YbRu_2Ge_2$, Phys. Rev. B **73**, 020407(R) (2006).

[11] E. W. Rosenberg, J.-H. Chu, J. P. Ruff, A. T. Hristov, and I. R. Fisher, Divergence of the quadrupole-strain susceptibility of the electronic nematic system $YbRu_2Ge_2$, Proc. Natl. Acad. Sci. USA **116**, 7232 (2019).

[12] C. Liu, Y.-D. Li, and G. Chen, Selective measurements of intertwined multipolar orders: Non-Kramers doublets on a triangular lattice, Phys. Rev. B **98**, 045119 (2018).

[13] G. Chen, Intrinsic transverse field in frustrated quantum Ising magnets: Physical origin and quantum effects, Phys. Rev. Res. **1**, 033141 (2019).

[14] C. Liu, C.-J. Huang, and G. Chen, Intrinsic quantum Ising model on a triangular lattice magnet $TmMgGaO_4$, Phys. Rev. Res. **2**, 043013 (2020).

[15] Y. Shen, C. Liu, Y. Qin, S. Shen, Y.-D. Li, R. Bewley, A. Schneidewind, G. Chen, and J. Zhao, Intertwined dipolar and multipolar order in the triangular-lattice magnet $TmMgGaO_4$, Nat. Commun. **10**, 4530 (2019).

[16] Y. Li, S. Bachus, H. Deng, W. Schmidt, H. Thoma, V. Hutanu, Y. Tokiwa, A. A. Tsirlin, and P. Gegenwart, Partial up-up-down order with the continuously distributed order parameter in the triangular antiferromagnet $TmMgGaO_4$, Phys. Rev. X **10**, 011007 (2020).

[17] S. Zheng, H. Wo, Y. Gu, R. L. Luo, Y. Gu, Y. Zhu, P. Steffens, M. Boehm, Q. Wang, G. Chen, and J. Zhao, Exchange-renormalized crystal field excitations in the quantum Ising magnet $KTmSe_2$, Phys. Rev. B **108**, 054435 (2023).

[18] M. M. Bordelon, E. Kenney, C. Liu, T. Hogan, L. Posthuma, M. Kavand, Y. Lyu, M. Sherwin, N. P. Butch, C. Brown, M. J. Graf, L. Balents, and S. D. Wilson, Field-tunable quantum disordered ground state in the triangular-lattice antiferromagnet $NaYbO_2$, Nat. Phys. **15**, 1058 (2019).

[19] R. Sarkar, P. Schlender, V. Grinenko, E. Haeussler, P. J. Baker, T. Doert, and H.-H. Klauss, Quantum spin liquid ground state

in the disorder free triangular lattice $NaYbS_2$, Phys. Rev. B **100**, 241116(R) (2019).

[20] P.-L. Dai, G. Zhang, Y. Xie, C. Duan, Y. Gao, Z. Zhu, E. Feng, Z. Tao, C.-L. Huang, H. Cao, A. Podlesnyak, G. E. Granroth, M. S. Everett, J. C. Neuefeind, D. Voneshen, S. Wang, G. Tan, E. Morosan, X. Wang, H.-Q. Lin *et al.*, Spinon Fermi surface spin liquid in a triangular lattice antiferromagnet $NaYbSe_2$, Phys. Rev. X **11**, 021044 (2021).

[21] Z. Zhang, J. Li, W. Liu, Z. Zhang, J. Ji, F. Jin, R. Chen, J. Wang, X. Wang, J. Ma, and Q. Zhang, Effective magnetic Hamiltonian at finite temperatures for rare-earth chalcogenides, Phys. Rev. B **103**, 184419 (2021).

[22] G. Ding, H. Wo, R. L. Luo, Y. Gu, Y. Gu, R. Bewley, G. Chen, and J. Zhao, Stripe order and spin dynamics in the triangular-lattice antiferromagnet $KErSe_2$: A single-crystal study with a theoretical description, Phys. Rev. B **107**, L100411 (2023).

[23] S. M. Avdoshenko, A. A. Kulbakov, E. Häußler, P. Schlender, T. Doert, J. Ollivier, and D. S. Inosov, Spin-wave dynamics in the $KCeS_2$ delafossite: A theoretical description of powder inelastic neutron-scattering data, Phys. Rev. B **106**, 214431 (2022).

[24] J. Rodríguez-Carvajal, Recent advances in magnetic structure determination by neutron powder diffraction, Phys. B (Amsterdam, Neth.) **192**, 55 (1993).

[25] W. Liu, Z. Zhang, J. Ji, Y. Liu, J. Li, X. Wang, H. Lei, G. Chen, and Q. Zhang, Rare-earth chalcogenides: A large family of triangular lattice spin liquid candidates, Chin. Phys. Lett. **35**, 117501 (2018).

[26] F. A. Cevallos, K. Stolze, T. Kong, and R. Cava, Anisotropic magnetic properties of the triangular plane lattice material $TmMgGaO_4$, Mater. Res. Bull. **105**, 154 (2018).

[27] C. Liu, F.-Y. Li, and G. Chen, Upper branch magnetism in quantum magnets: Collapses of excited levels and emergent selection rules, Phys. Rev. B **99**, 224407 (2019).

[28] S. Voleti, F. D. Wandler, and A. Paramekanti, Impact of gapped spin-orbit excitons on low energy pseudospin exchange interactions, arXiv:2303.04169.

[29] K. Nakajima, S. Ohira-Kawamura, T. Kikuchi, M. Nakamura, R. Kajimoto, Y. Inamura, N. Takahashi, K. Aizawa, K. Suzuya, K. Shibata *et al.*, AMATERAS: A cold-neutron disk chopper spectrometer, J. Phys. Soc. Jpn. **80**, SB028 (2011).

[30] R. Ewings, A. Buts, M. Le, J. van Duijn, I. Bustinduy, and T. Perring, HORACE: Software for the analysis of data from single crystal spectroscopy experiments at time-of-flight neutron instruments, Nucl. Instrum. Methods Phys. Res., Sect. A **834**, 132 (2016).

[31] J. Lass, H. Jacobsen, K. M. L. Krighaar, D. Graf, F. Groitl, F. Herzog, M. Yamada, C. Kägi, R. A. Müller, R. Bürge *et al.*, Commissioning of the novel continuous angle multi-energy analysis spectrometer at the Paul Scherrer Institut, Rev. Sci. Instrum. **94**, 023302 (2023).

[32] J. Lass, H. Jacobsen, D. G. Mazzone, and K. Lefmann, MJOLNIR: A software package for multiplexing neutron spectrometers, SoftwareX **12**, 100600 (2020).

[33] K. W. H. Stevens, Matrix elements and operator equivalents connected with the magnetic properties of rare earth ions, Proc. Phys. Soc. A **65**, 209 (1952).

[34] G. J. Bowden, D. S. P. Bunbury, and M. A. H. McCausland, Crystal fields and magnetic anisotropy in the molecular field approximation. I. General considerations, J. Phys. C **4**, 1840 (1971).

[35] M. Rotter, Using McPhase to calculate magnetic phase diagrams of rare earth compounds, J. Magn. Magn. Mater. **272-276**, E481 (2004).

[36] S. Chi, P. Dai, T. Barnes, H. J. Kang, J. W. Lynn, R. Bewley, F. Ye, M. B. Maple, Z. Henkie, and A. Pietraszko, Inelastic neutron scattering study of crystal field levels in $PrOs_4As_{12}$, Phys. Rev. B **77**, 094428 (2008).

[37] Y. Qin, Y. Shen, C. Liu, H. Wo, Y. Gao, Y. Feng, X. Zhang, G. Ding, Y. Gu, Q. Wang, S. Shen, H. C. Walker, R. Bewley, J. Xu, M. Boehm, P. Steffens, S. Ohira-Kawamura, N. Murai, A. Schneidewind, X. Tong *et al.*, Field-tuned quantum effects in a triangular-lattice Ising magnet, Sci. Bull. **67**, 38 (2022).